Journal of Alloys and Compounds 509 (2011) 8641–8648

Contents lists available at ScienceDirect

Journal of Alloys and Compounds

journal homepage: www.elsevier.com/locate/jallcom

Effect of accumulated shear on the microstructure and morphology of severely deformed $Cu_{60}Zr_{30}Ti_{10}$ metallic glass

Sándor Hóbor, Zsolt Kovács*, Ádám Révész

Department of Materials Physics, Eötvös University, P.O.B. 32, Budapest H-1518, Hungary

ARTICLE INFO

Article history:
Received 5 April 2011
Received in revised form 7 June 2011
Accepted 13 June 2011
Available online 21 June 2011

Keywords:
Metallic glasses
Heat conduction
Thermodynamic modeling
Microstructure
Nanostructured materials

ABSTRACT

$Cu_{60}Zr_{30}Ti_{10}$ metallic glass sample was subjected to different amount of continuous rotational straining by high pressure torsion. Deformation dependent morphology, microstructural and thermal properties were characterized by scanning electron microscopy, synchrotron radiation, X-ray diffraction, and calorimetry, respectively. In order to estimate the temperature rise in the metallic glass during high pressure torsion, quasi three-dimensional heat conduction equation with a source term was considered. Solutions indicate that the final temperature strongly depends on the total amount of plastic deformation while details of the microstructure are mainly determined by the balance between the local shear rate and temperature.

1. Introduction

Bulk metallic glasses (BMGs) lacking long range order and microstructural faults such as grain boundaries, are attaining increasing number of applications in different industrial fields. However, shear band formation during deformation below the glass transition temperature (T_g) limits the plasticity and therefore also the possible applications of BMGs [1]. In narrow regions with a thickness of ~10 nm the plastic flow is extremely localized, the atomic mobility is remarkably enhanced and the temperature rises locally resulting in shear softening that leads to the failure of the material [1–4]. As the external temperature approaches the glass transition temperature (T_g), the localized inhomogeneous deformation mode shows a transition to homogeneous viscous flow [4]. The plasticity of metallic glasses can be enhanced by dispersing the macroscopic deformation among large number of competitive shear bands either by surface constraints techniques [5,6], or by introducing inhomogeneity into the microstructure [7,8].

Cu-based metallic glasses with high glass forming ability (GFA) and good mechanical properties, such as large tensile strength and intrinsic plasticity are attaining increasing interest [9–11]. The remarkably high GFA of Cu–Zr alloy allows casting in bulk form exceptionally among binary systems [12]. Besides, Eckert and co-workers developed Cu–Zr-based BMGs, which polymorphically precipitate nanocrystals during tensile deformation. The formation of such structural heterogeneities, e.g. plastically deformable intermetallic phases, hampers shear band generation, may dictate the strain–stress behavior of the BMG and results in macroscopically detectable plastic strain and work hardening [13,14]. Recently, high pressure torsion (HPT) [15] based on severe plastic deformation was also successfully applied to induce nanocrystals in amorphous alloys [16–18]. During this process, a disk-shaped sample placed between two anvils is subjected to compressive force and concurrent torsional straining for several revolutions, where hydrostatic conditions are fulfilled in the interior of the disk [19,15]. It was shown, that in spite of the strong radial dependence of the strain, the microstructure and the correlating mechanical properties [20], e.g. the value of the Vickers-hardness is almost constant along the diameter after 5 turns in case of crystalline materials [21,22]. In addition the Vickers-hardness was found to be identical in different horizontal layers of each disk [21].

Egami and co-workers recently examined the structure of HPT-deformed Cu–Zr–Al bulk metallic glass disks using high-energy X-ray diffraction, comparing atomic pair distribution function (PDF) from deformed and undeformed reference samples [23]. The observed difference indicates that both short and long inter-atomic distances are altered by deformation. The changes in PDF are opposite to the changes observed for structural relaxation, and suggest that deformation significantly increases the fictive temperature of a glass, effectively rejuvenating the structure.

In a recent study, the observed morphological and microstructural features introduced by HPT of an amorphous $Cu_{60}Zr_{30}Ti_{10}$

* Corresponding author. Tel.: +36 1 372 2823; fax: +36 1 372 2811.
E-mail address: kovacszs@metal.elte.hu (Z. Kovács).

0925-8388/$ – see front matter © 2011 Elsevier B.V. All rights reserved.
doi:10.1016/j.jallcom.2011.06.046

alloy were interpreted by temperature profiles obtained from a simple model based on one-dimensional heat-conduction [24,25]. Later the effect of the instrumental parameters on the temperature rise was discussed in terms of a quasi three-dimensional model [26], and the role of the most important parameter, i.e. the shear rate on the microstructure and thermal stability was investigated in detail [27]. In the present study the effect of accumulated shear strain on the microstructure and morphology of amorphous $Cu_{60}Zr_{30}Ti_{10}$ alloy developed during HPT is demonstrated and explained in terms of the maximum temperature achieved during the process.

2. Experimental

An ingot of nominal composition of $Cu_{60}Zr_{30}Ti_{10}$ was prepared by induction melting of high purity (99.9%) Cu, Zr and Ti metals. Ribbon was obtained by using single roller melt spinning technique in inert atmosphere with a Cu-wheel rotating at a tangential velocity of 3800 rpm. Subsequently the fully amorphous ribbon has been cut into flakes and then placed between HPT-anvils and compressed into several porosity free, round shaped disks with a radius of $R = 2.8$ mm and a maximum thickness of $L = 250$ μm under an applied pressure of 6 GPa, with various N number of rotations. Torsion straining was performed at $t_{rev} = 1$ min revolution time. The accumulated shear strain for torsion deformation at a distance $r < R$ and at a time t can be represented by

$$\gamma(r,t) = \frac{2\pi Nr}{L} = \frac{2\pi tr}{Lt_{rev}} \quad (1)$$

According to the number of rotations three different samples, $N = 0.5$, $N = 5$ and $N = 10$ have been involved in the investigations.

Microstructure was examined by powder X-ray diffraction (XRD) on a Philips X'pert diffractometer using Cu Kα radiation in the range of 30–80° in θ–2θ geometry. Position sensitive 2D X-ray diffraction measurements were carried out at the ID-11 beamline of the European Synchrotron Radiation Facility (ESRF) using monochromatic photons of 90 keV. The X-ray beam with a size of 10 μm × 10 μm passed through the sample in transmission mode. The sample-detector distance was calibrated by a LaB_6 polycrystalline specimen. The disks were mapped by taking a series of 2D diffraction patterns along a diameter with a step size of 0.3 mm, using a charge coupled device (CCD) detector (Bruker) coupled to an image intensifier, with an exposure time of 15 s. The two-dimensional patterns were integrated, after dark-current and spatial distortion correction using Fit-2D software [28].

Morphology studies were performed on a Philips XL 30 scanning electron microscopy (SEM) in backscattered electron (BSE) mode on the mechanically polished cross-section of the disks, while the compositional changes were quantitatively determined by energy dispersive X-ray (EDX) analysis with a relative accuracy of 3%.

A Perkin Elmer power compensated differential scanning calorimeter (DSC) was applied to investigate the thermal behavior and crystallization applying continuous heating experiments performed at scan rate of 40 K/min. All measurements were carried out under argon atmosphere. The temperature and the enthalpy were calibrated by using pure In and Al. Each measurement was followed by a second run in order to obtain the baseline.

3. Results

Fig. 1 presents the XRD measurements taken on the surface of the HPT-disks subjected to different rotational straining ($N = 0.5$, $N = 5$ and $N = 10$). In general, each pattern averaging the X-ray scattering from the whole surface is dominated only by a broad symmetric halo at around $2\Theta = 41°$, without any visible Bragg-peaks, similarly to the as-quenched amorphous ribbon (see Fig. 1).

The microstructural differences associated with the different amount of rotational straining at the center and at the perimeter of each disk are visualized in the SEM BSE images (Fig. 2a–c). As a consequence of compaction and simultaneous shearing the individual ribbon pieces cannot be resolved even in the least deformed $N = 0.5$, see Fig. 2a. The cross-section is homogeneous along the diameter and characterized by several bunches of parallel very thin elongated dark grey bands with a length of 10–15 μm dispersed in the amorphous matrix close to the rotational axis as well as at the perimeter.

Higher amount of strain results in significantly different morphology for the $N = 5$ sample (Fig. 2b), i.e. the center of the disk is fragmented by a couple of branching cracks aligning parallel to the sample surface, while several elongated dark grey blocks with a length of around 20–30 μm are dispersed in the matrix. At the perimeter their size (~5–10 μm) and density are much smaller than close to the rotation axis. Quantitative EDX analysis revealed that the composition of the matrix ($Cu_{60}Zr_{30}Ti_{10}$) is similar to that of the as-quenched alloy, while the blocks are slightly enriched in Cu ($Cu_{62}Zr_{20}Ti_{18}$).

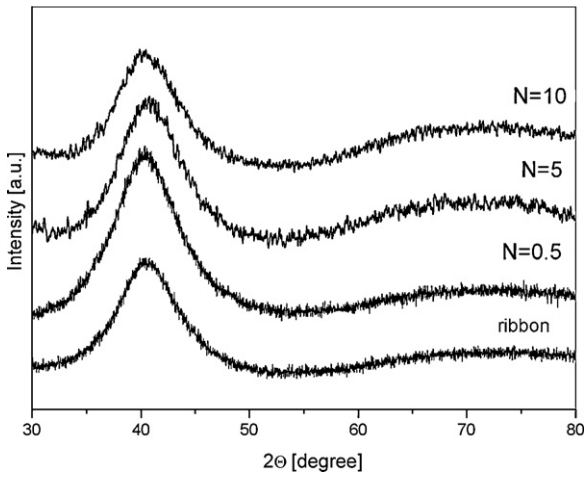

Fig. 1. XRD patterns of the as-quenched $Cu_{60}Zr_{30}Ti_{10}$ ribbon and HPT disks subjected to different amount of torsional deformation ($N = 0.5$, $N = 5$ and $N = 10$).

Further deformation changes the average size and structure of these particles, the $N = 10$ sample contains several robust blocks of 25–50 μm (Fig. 2c), with eutectic-like decomposed morphology. A typical devitrified block decomposed into dark Ti-rich ($Cu_{57}Zr_7Ti_{35}$) and light (almost Ti-free $Cu_{78}Zr_{19}Ti_3$) zones is shown enlarged in the inset. At larger radius the microstructure is more homogeneous, with fewer cracks and smaller blocks characterize the cross-section.

Fig. 3 summarizes synchrotron experiments carried out on the amorphous alloy and on samples $N = 5$ and $N = 10$. As seen the transmission X-ray diffractogram of the as-quenched ribbon is dominated only by two broad symmetric halos centered at around 28 nm^{-1} and 47 nm^{-1}, respectively. As an effect of shear deformation some of the patterns corresponding to the $N = 5$ sample exhibit sharp crystalline peaks as well, indicating a strong microstructural inhomogeneity along the diameter. The dominant crystalline peaks characterizing mainly the central region of the disk can be indexed as hexagonal Cu_2ZrTi ($p6_3/mmc$, $a = 0.505$ nm, $c = 0.82$ nm). Subsequent deformation ($N = 10$) results in the shift of the first amorphous halo by approximately +0.5 nm^{-1}. Simultaneously the Bragg-peaks practically disappear at each measurement point. Note that the different intensity of the amorphous halos corresponding to different positions is a consequence of the variation in sample thickness.

Based on the high stability of the synchrotron beam, the amorphous content along the diameter of the $N = 5$ and $N = 10$ disks can be determined by analyzing the individual XRD patterns. During this procedure the amorphous fraction (Ψ) as a function of the radius r can be approximated as

$$\Psi(r) = \alpha(r)\frac{I^r_{disk}(Q_{ref})}{I_{ribbon}(Q_{ref})} \quad (2)$$

where I_{ribbon} and I^r_{disk} are the intensity of the diffraction patterns at the largest measured Q value ($Q_{ref} = 110$ nm^{-1}) for the ribbon and for the disk at r, respectively. It is noted that the scattered intensity at Q_{ref} is practically proportional to the transmitted sample thickness, i.e. $I^r_{disk}(Q_{ref})/I_{ribbon}(Q_{ref}) = d_{disk}(r)/d_{ribbon}$, where $d_{disk}(r)$ and d_{ribbon} are the thickness of the disk at r and the amorphous ribbon, respectively. The $\alpha(r)$ coefficient of Eq. (2) was determined as the

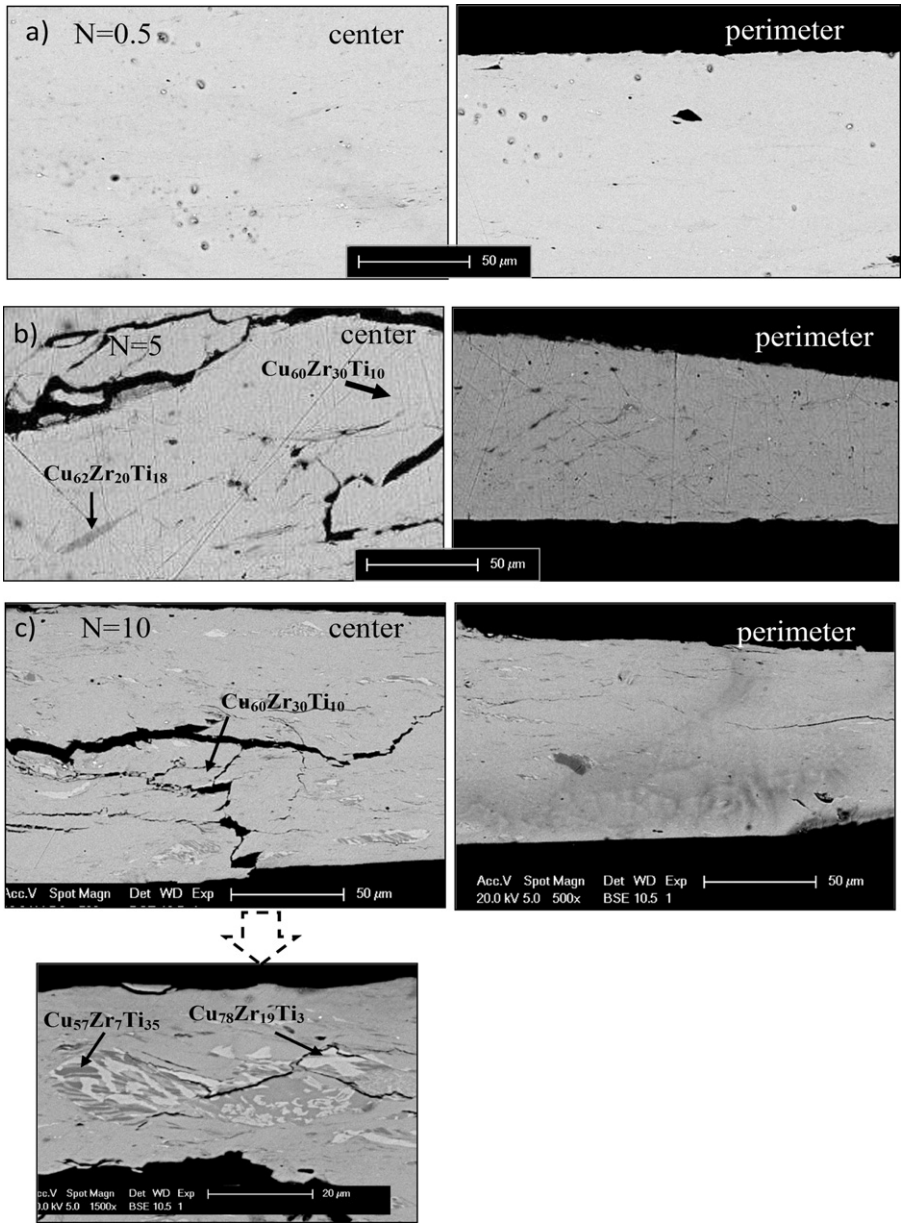

Fig. 2. Couples of SEM BSE images of the cross-section of HPT-disks subjected to different torsional deformation (a) $N = 0.5$, (b) $N = 5$ and (c) $N = 10$. Images of the left and right column are taken at the center and perimeter of the corresponding HPT disks, respectively. The inset shows enlargement of a devitrified and decomposed block in $N = 10$ disk.

maximum value for which the $I^r_{\text{disk}}(Q) - \alpha(r) \cdot I_{\text{ribbon}}(Q) > 0$ condition is fulfilled for all Q, as presented in Fig. 4a and b. The calculated values of the amorphous content indicate a discrepancy for samples $N = 5$ and $N = 10$ (Fig. 5), i.e. $\Psi(r)$ decreases monotonically with increased amount of torsional deformation to 72% and 49%, respectively. At the same time, the effect of $\Psi(r)$ along the diameter is remarkably higher for the less-deformed specimen, while for the most deformed disk $\Psi(r)$ fluctuates in the range of the experimental error.

Continuous heating DSC curves corresponding to the different parts of the HPT disks and the amorphous alloy are plotted in Fig. 6. The as-quenched ribbon presents an endothermic glass transition (T_g) followed by two sharp exothermic peaks with characteristic temperatures of T_1 and T_2. As a consequence of continuous shear, T_g becomes less and less pronounced with increasing deformations. Albeit the endothermic effect is practically unchanged for the whole $N = 0.5$ disk, nevertheless it remains barely noticeable for the central parts of $N = 5$ and $N = 10$ disks and almost disappears for the perimeters. At the same time T_1 shifts gradually to higher temperature (from 750 K to 761 K) with increasing deformation, indicating increasing thermal stability, while T_2 slightly decreases from 819 K to 814 K. Transformation enthalpies (ΔH_1, ΔH_2) obtained as the area of the first and second exothermic peaks are plotted as a fraction of the values corresponding to the as-quenched amorphous ribbon (Fig. 7a and b). As seen, severe shearing occurs a significant drop of both ΔH_1 and ΔH_2, characterizing all regions of the least deformed disk ($N = 0.5$). However, after subsequent deformation ($N = 5$ and $N = 10$ samples) the perimeter and the center of the disks behave differently. On one hand, ΔH_1 remains almost unchanged in the perimeter (saturating at ~80%) but ΔH_2 drops down to ~50%. On the other hand, for the central parts of the $N = 5$ and $N = 10$ samples the area of both exothermic peaks are significantly smaller compared to $N = 0.5$, however, a detectable increase is observed for the most deformed state, especially in ΔH_2. As a summary, Fig. 7c presents the evolution of total enthalpy released ($\Delta H_{\text{tot}} = \Delta H_1 + \Delta H_2$) as a function of the number of rotations.

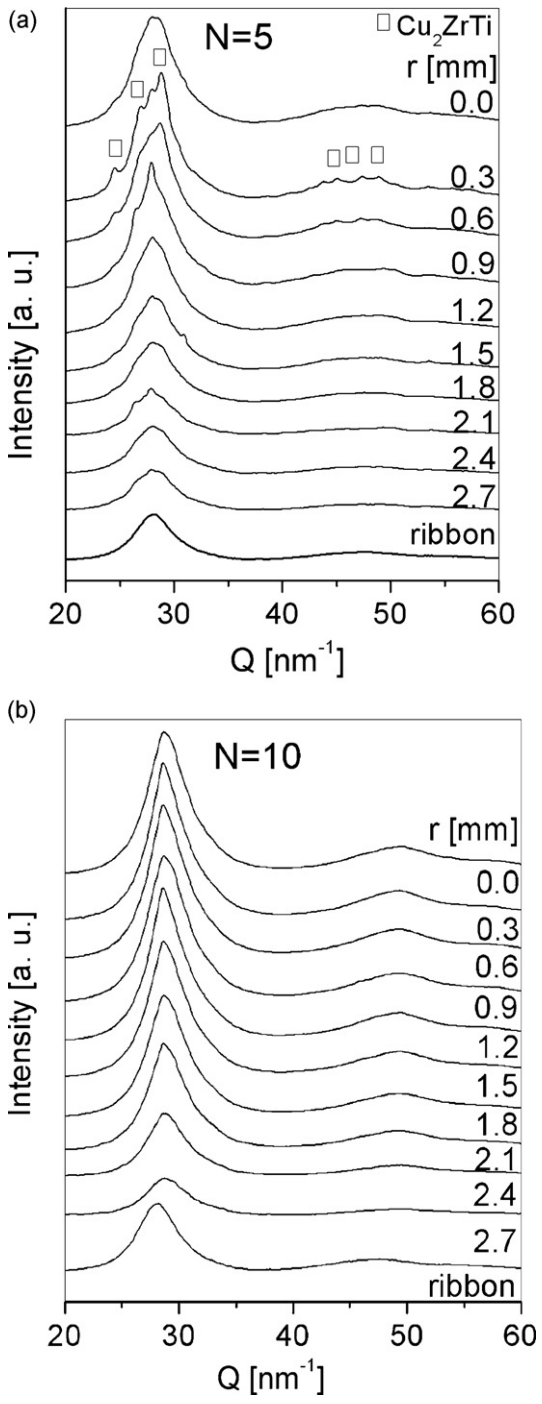

Fig. 3. Series of transmission synchrotron X-ray diffractograms taken perpendicular through the disk plane of the (a) $N=5$ and (b) $N=10$ HPT samples at different distances (r) from the center. Diffractogram of the fully amorphous as-quenched ribbon is also depicted as a reference.

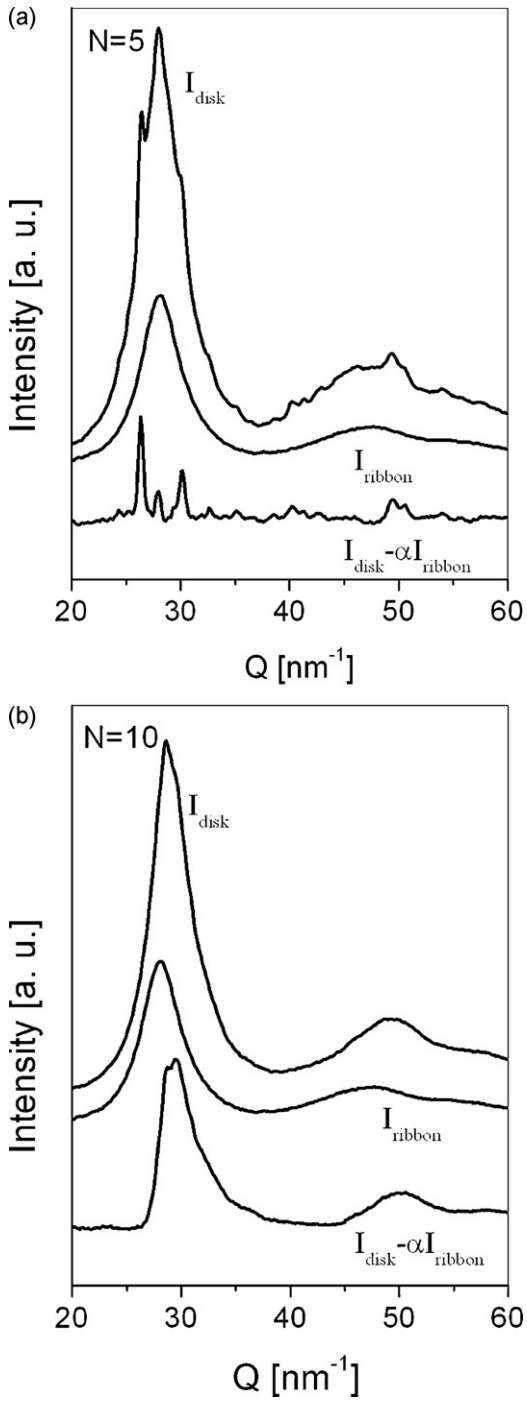

Fig. 4. X-ray diffractograms taken by high brilliance synchrotron radiation of the as-quenched ribbon (I_{ribbon}) and HPT disks (I_{disk}) with $N=5$ and $N=10$ torsional deformation. By subtracting the amorphous component of the ribbon with a proper weight (α), the residual diffraction ($I_{disk}-\alpha I_{ribbon}$) of the remaining (nano)crystallite phase mixtures is resolved.

4. Discussion

As was demonstrated by SEM and DSC, the increasing amount of accumulated shearing during high pressure torsion of the $Cu_{60}Zr_{30}Ti_{10}$ amorphous alloy resulted in significantly different microstructure, morphology and thermal behavior. Though the characteristic features of $N=0.5$ disk slightly differ from those of the as-quenched alloy, further shearing ($N=5$ and $N=10$ samples) drastically changes the morphology (see Fig. 2). Large crystalline blocks embedded in the amorphous matrix dominate the regions close to the rotational axis (see Fig. 2b and c), nevertheless in the perimeter the size of these blocks decreases drastically for both samples. As can be observed, the detailed characteristics of these blocks in the central areas are strongly diverse, i.e. in the less deformed $N=5$ disk they are elongated (with a maximum length of 15–20 μm) and exhibit homogeneous dark grey colour in the image. The average composition of these blocks is only slightly different from the amorphous matrix ($Cu_{62}Zr_{20}Ti_{18}$). On contrary, the blocks are notably larger (25–50 μm) in the most deformed

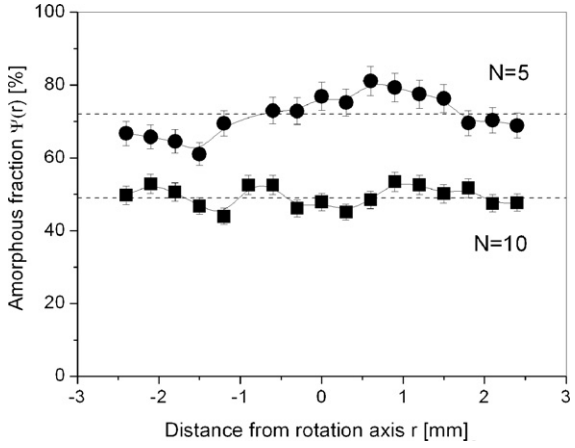

Fig. 5. Volume fraction of the amorphous component, $\Psi(r)$, obtained by synchrotron X-ray diffraction along the diameter of the $N = 5$ and $N = 10$ HPT disks.

$N = 10$ sample, composed of a eutectic-like decomposed structure of dark Ti-rich ($Cu_{57}Zr_7Ti_{35}$) and light Ti-free ($Cu_{78}Zr_{19}Ti_3$) zones (see Fig. 2c inset). The corresponding transmission X-ray diffractograms taken on the two most deformed samples have surprising features (see Fig. 3). While the series belonging to the $N = 5$ disk confirm the formation of a stable hexagonal phase (Cu_2ZrTi) close to the rotation axes (see Fig. 3a), the $N = 10$ disks seems to be homogeneous along the diameter (Fig. 3b).

The above conflict obtained between the SEM images and the synchrotron data, however, can be resolved by a recently developed three-dimensional thermoplastic model based on heat conduction [26]. In brief, the temperature evolution in the disk-shape sample

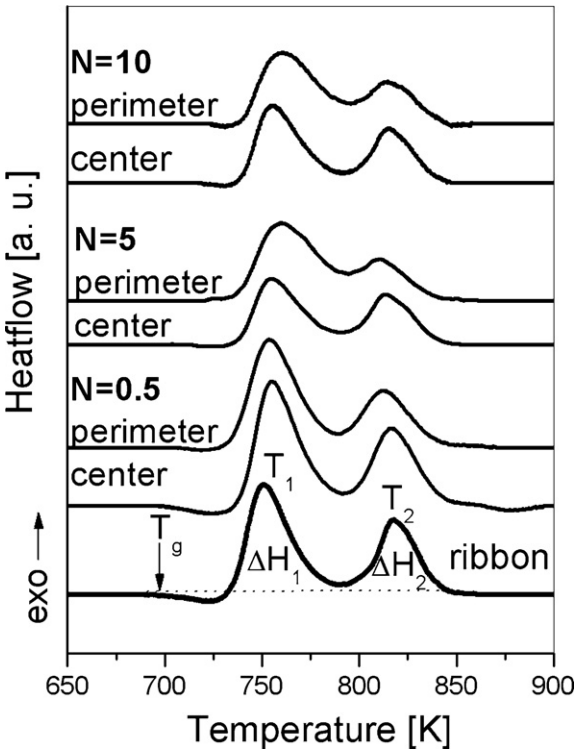

Fig. 6. DSC thermograms of the as-quenched $Cu_{60}Zr_{30}Ti_{10}$ ribbon and HPT disks processed by different amount of torsional deformation.

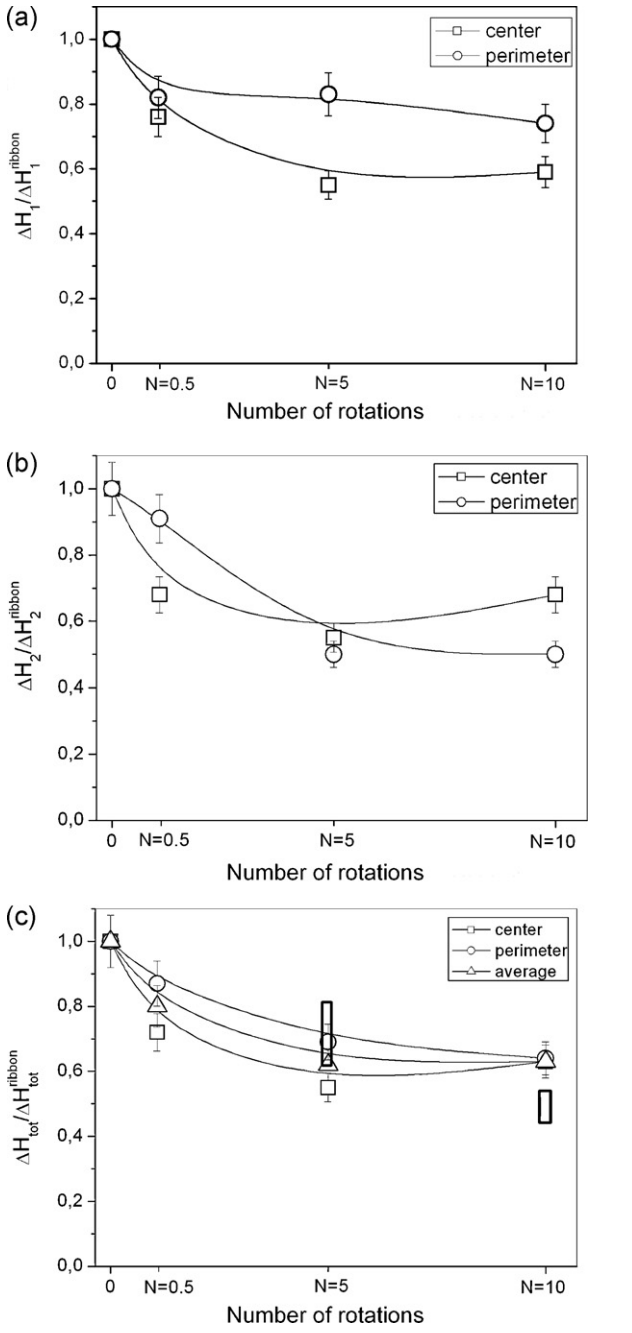

Fig. 7. Normalized enthalpies for the (a) first, $\Delta H_1/\Delta H_1^{\text{ribbon}}$, (b) second, $\Delta H_2/\Delta H_2^{\text{ribbon}}$ and (c) for the sum of the first and second $\Delta H_{\text{tot}}/\Delta H_{\text{tot}}^{\text{ribbon}}$ DSC peaks corresponding to the center and the perimeter of the HPT disks. Rectangular boxes indicate the range of the different amorphous volume fractions, Ψ, obtained from synchrotron diffraction patterns.

during the HPT-process can be derived from the heat conduction equation with a source term, $S(r,t)$:

$$c(r)\rho(r)\frac{\partial T(r,t)}{\partial t} - \Delta(k(r)T(r,t)) = S(r,t) \quad (3)$$

where c, ρ and k are the heat capacity, the density and the thermal conductivity, respectively. The heat source term in the model, $S(r,t)$,

Table 1
Material parameters introduced in the numerical model, heat conductivity (k), heat capacity (c), density (ρ), glass transition temperature (T_g) and flow stress (τ_f).

	k [W m^{-1} K^{-1}]	c [J kg^{-1} K^{-1}]	ρ [kg m^{-3}]	T_g [K]	τ_f [GPa]
$Cu_{60}Zr_{30}Ti_{10}$	7.7	420	6125	710	0.104
Steel	30	460	7800	–	–
Air	0.024	1000	1.2	–	–

is a plastic deformation induced heat release which is kept zero outside the BMG disk and can be given inside the sample as follows:

$$S(r,t) = \begin{cases} \tau_f \dfrac{\partial \gamma(r,t)}{\partial t} & \text{if } T < T_g \\ \eta(T)\left(\dfrac{\partial \gamma(r,t)}{\partial t}\right)^2 & \text{if } T > T_g \end{cases} \quad (4)$$

where τ_f, γ and $\eta(T)$ are the flow stress, the shear strain and the temperature dependent viscosity, respectively. In the model the parameters of the Vogel–Fulcher formula, $\eta(T) = \eta_0 \exp(QT_{VF}/(T - T_{VF}))$ [29,30], were adjusted in order to satisfy the boundary condition:

$$\eta(T)\frac{d\gamma(r)}{dt}\bigg|_{T=T_g, r=R} = \tau_f \quad (5)$$

as $T_{VF} = 620$ K, $Q = 0.84$, $\eta_0 = 590$ Pa s.

The material parameters for the $Cu_{60}Zr_{30}Ti_{10}$ disk [3,7], steel anvils and air applied in the numerical calculations are listed in Table 1. Noteworthy that the material parameters of widely investigated metallic glasses have only a slight influence on the temperature evolution [26]. The more detailed description of the model is given elsewhere [26].

The temperature profiles along the diameter calculated at different times during the HPT process are plotted in Fig. 8a. As seen, the temperature has a local minimum at the center ($r = 0$) at each time step, furthermore it increases with increasing strain rate up to $r \approx 1.3$ mm, however, a significant decline is observed at the perimeter. We note that this decline is a general feature due to the enhanced heat dissipation at the perimeter of the disk, but details of the profiles depend on the geometry of the HPT anvil [26]. For the disk of $N = 0.5$ rotation the temperature at the perimeter is lower by 10 K than in the center. As shearing goes on, the temperature rises gradually in the whole disk, though flattening of the profiles is observed once T_g is reached. After $N = 10$ revolution the maximum temperature is 723 K and at the edge $T = 719$ K. As seen on the temperature evolution curve corresponding to $r = 0$ during the HPT process, T_g is reached after $t^* \sim 50$ s of continuous rotational shearing, thereafter the rate of the temperature rise decreases abruptly, yielding a temperature saturation at around 720 K (Fig. 8b). Full circles denote the maximum temperatures achieved at the end of the HPT processes for the three experimentally studied samples. Accordingly the temperature increases by ~350 K, but remains below the glass transition temperature for the $N = 0.5$ disk. However, for longer deformation ($N = 5$), the temperature exceeds T_g, while subsequent rotational shearing ($N = 10$) represents a longer annealing slightly above T_g. Radial dependent temperature evolution curves of the perimeter ($r = 2$–2.8 mm) indicate that the glass transition happens barely before the end of the $N = 5$ process (see the inset of Fig. 8b).

Based on the calculated temperature profiles (see Fig. 8a), the viscosity (η) can be obtained from the Vogel–Fulcher formula. Fig. 9 presents the inverse of the viscosity, $\eta^{-1}(r)$, along the radius for the final state of each HPT procedures. Since the $\eta^{-1}(r)$ correlates with the atomic mobility [31], the depicted curves in Fig. 9 characterize the differences in the local atomic mobilities of the different samples. Accordingly, as the temperature remains below T_g during $N = 0.5$ rotation, the mobility is very small compared to the other two disks. For the $N = 5$ and $N = 10$ samples η^{-1} is in the order of magnitude of 10^{10} Pa^{-1} s^{-1} associated with a strong radial dependence. The value of η^{-1} is practically constant in the interior region of the disk (from $r = 0$ mm to $r \sim 1.5$ mm), though it sharply decreases at the perimeter. In the center $\eta^{-1} = 2.5 \times 10^{10}$ Pa^{-1} s^{-1}

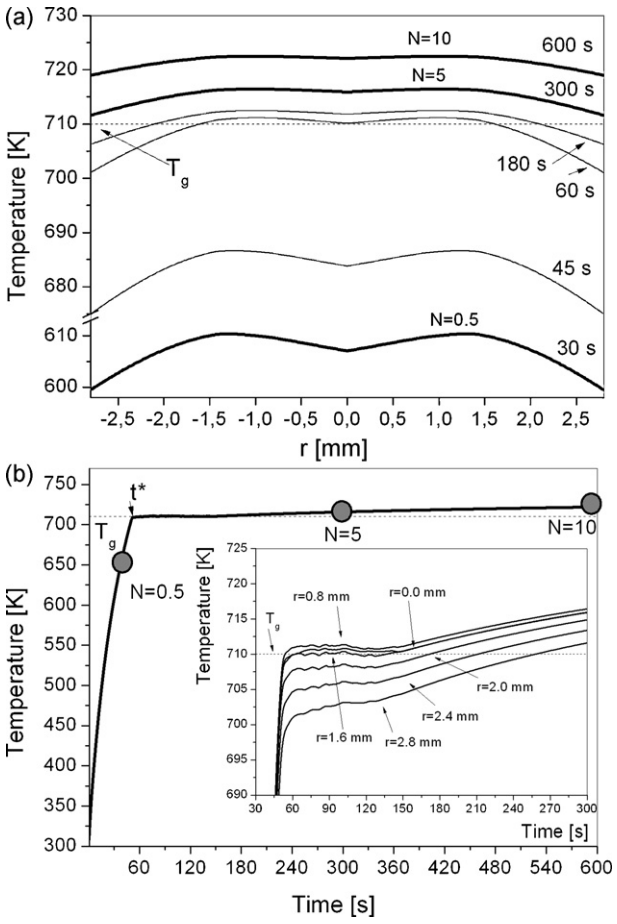

Fig. 8. (a) Temperature profiles obtained from the heat-conduction equation (Eq. (3)) along the diameter of the HPT-disk. Bold curves indicate the profiles corresponding to the experimentally investigated states ($N = 0.5$, 5 and 10). (b) Temperature evolution curves as a function of processing time. t^* denotes the time at which the temperature reaches the glass transition (T_g). Full circles denote the $N = 0.5$, $N = 5$ and $N = 10$ states. The inset confirms a relatively small inhomogeneity in the temperature near (T_g).

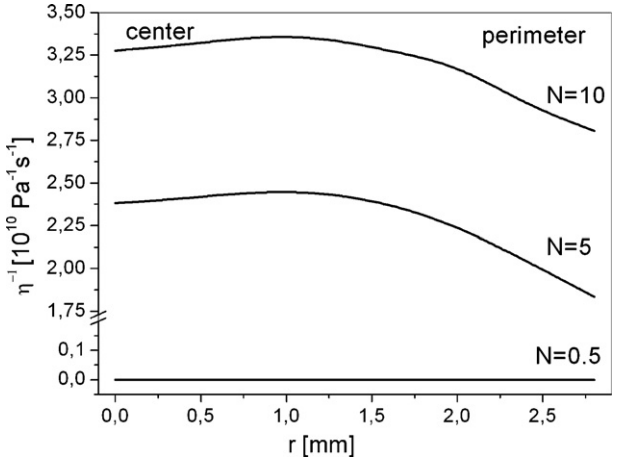

Fig. 9. Variation of the inverse of the viscosity (η^{-1}) as a function of the distance from the center (r) obtained from the numerical thermo-mechanical simulations.

and $\eta^{-1} = 3.25 \times 10^{10}\,\mathrm{Pa^{-1}\,s^{-1}}$, while in the perimeter it decreases to $1.75 \times 10^{10}\,\mathrm{Pa^{-1}\,s^{-1}}$ and $2.8 \times 10^{10}\,\mathrm{Pa^{-1}\,s^{-1}}$ for the $N = 5$ and $N = 10$ samples, respectively.

These results obtained from the numerical solution of the three-dimensional thermoplastic model give a hint for a better comprehension of the morphology evolved in the different stages of the HPT process. Until the temperature remains below T_g, i.e. $t < t^* \approx 50$ s (during the total $N = 0.5$ process, see Fig. 8a and b), the plastic deformation is localized in shear bands, resulting in local temperature rise in small volumes [1–4]. As a consequence, plenty of nuclei may form in the amorphous matrix near these locally heated deformation zones, that partly coalesce in the plane of shear deformation, forming bunches of elongated crystalline bands, as seen in Fig. 2a. The nucleation of these nanocrystals yields the drop of ΔH_{tot} compared to the as-quenched amorphous state (Fig. 7c).

As seen in Fig. 8, the temperature is above the glass transition during the majority of the shearing (~250 s and ~550 s for the samples $N = 5$ and $N = 10$, respectively), meaning homogeneous viscous flow deformation [4]. Accordingly, the HPT-process can be divided into two distinct stages on the basis of the deformation mode. During the first stage plenty of nuclei form in the entire disk. Then, as the temperature exceeds T_g two competing effects dominate the evolving microstructure. On one hand, high temperature, low viscosity and high atomic mobility all enhance the diffusion paths, hereby support the growth of nanocrystals and the devitrification of the amorphous matrix. On the other hand, the growth and coalescence of the nanocrystals is strongly limited by the persistent shear especially in the perimeter of the disks [32]. So that the formation of the large blocks is favoured only in regions of higher temperature and smaller strain rate.

Accordingly, the microstructure of the less deformed central region and heavily sheared perimeter develops differently. Due to higher atomic mobility, the nuclei continuously grow and coalesce into robust crystalline blocks characterizing the center of the $N = 5$ sample (see Fig. 2b), which decompose into Ti-rich and Ti-free zones during longer deformation above T_g (see the image for $N = 10$ in Fig. 2c). Since no Bragg-peaks can be visualized in the corresponding diffractograms (Fig. 3b), the coherent domain size of these decomposed zones is definitely smaller compared to that of the blocks of the $N = 5$ disks. However, the subtraction procedure applied for determining the amorphous fraction (Fig. 4), provides the $I^r_{\mathrm{disk}} - \alpha I_{\mathrm{ribbon}}$ residual diffractograms characterized by broad crystalline peaks for $N = 10$, as presented in Fig. 10a. These strongly overlapping crystalline peaks (see, e.g. $r = -0.3$ mm) compile a halo which is centered at higher Q-value compared to I_{ribbon} (see Fig. 4b).

At the same time, the coalescence of the nuclei is strongly limited by the persistent shear and lower mobility at the perimeter, yielding a more homogenous microstructure of much smaller blocks embedded in the amorphous matrix (Fig. 2c). Moreover, nano-sized crystalline inclusions were also observed by transmission electron microscope in a recent paper [24], which are hardly detectable by X-ray scattering (Figs. 3a and b and 10b).

The shear induced annealing resulting in the formation of the crystalline blocks is in accordance with the decreasing contribution of T_g as the deformation is increased (see the DSC thermograms in Fig. 6). If it is assumed that total heat release ($\Delta H_1 + \Delta H_2 = \Delta H_{\mathrm{tot}}$) refers only to the amorphous–crystalline transition [33], the function $\Delta H_{\mathrm{tot}}/\Delta H^{\mathrm{ribbon}}_{\mathrm{tot}}$ plotted in Fig. 7c should match with the values (Ψ) evaluated from the synchrotron measurements. Indeed, the general decaying tendency of $\Delta H_{\mathrm{tot}}/\Delta H^{\mathrm{ribbon}}_{\mathrm{tot}}$ with the number of rotations is evident, as was also obtained from Fig. 5. Moreover, the fluctuations in the value of Ψ (denoted by rectangular in Fig. 7c) is comparable to the variation of $\Delta H_{\mathrm{tot}}/\Delta H^{\mathrm{ribbon}}_{\mathrm{tot}}$ for the $N = 5$ and $N = 10$ states. By analyzing the data in detail, however, it is seen that $\Delta H_{\mathrm{tot}}/\Delta H^{\mathrm{ribbon}}_{\mathrm{tot}}$ is slightly higher than Ψ for $N = 10$ which might correspond to the increased grain-boundary enthalpy of developing nano-size crystals due to the heavy shear deformation.

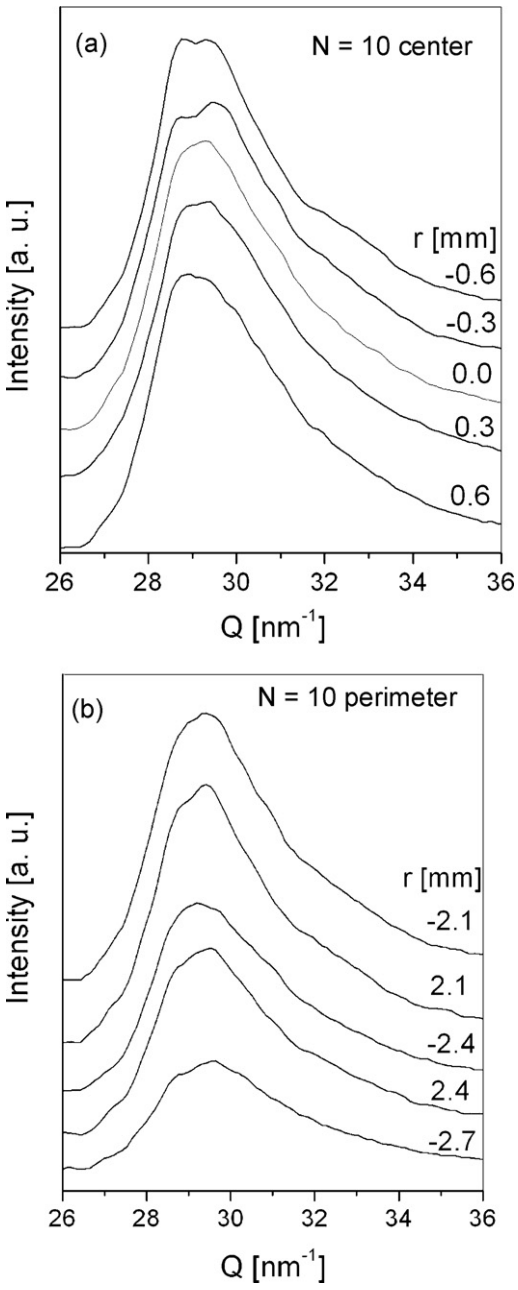

Fig. 10. Residual X-ray diffractograms ($I_{\mathrm{disk}} - \alpha I_{\mathrm{ribbon}}$) taken on the center (a) and the perimeter (b) of the $N = 10$ HPT disk.

5. Conclusions

Numerical calculations based on quasi three-dimensional heat conduction equation have satisfactorily explained the microstructural differences and thermal behavior of amorphous $Cu_{60}Zr_{30}Ti_{10}$ alloy subjected to different amount of rotational straining by HPT.

Scanning electron microscopy study has shown that the center of the $N = 5$ HPT disk is abundant in elongated blocks (15–20 μm) which transforms into more robust, eutectic-like morphology after further deformation ($N = 10$). At larger radius of the disks the microstructure is more homogeneous. Based on high stability synchrotron X-ray diffraction, we found that these blocks contain (nano)crystallites and the amorphous con-

tent of the $N = 5$ and $N = 10$ disks was determined as 72% and 49%, respectively, in accordance with the calorimetric data.

According to the temperature evolution profiles obtained from the numerical model, the HPT process may be divided into distinct stages. For small amount of total plastic deformation ($N = 0.5$) the temperature remains below the glass transition in the entire disk, while for larger deformation the glass transition temperature is exceeded in the samples ($N = 5$ and $N = 10$).

Despite the relatively small temperature differences developed across the diameter of the HPT disk, the remarkable different microstructure is explained by the competition of local strain rate and thermal mobility.

Acknowledgements

The European Union and the European Social Fund have provided financial support to the project under the grant agreement no. TÁMOP 4.2.1./B-09/1/KMR-2010-0003. We appreciate the support of the Hungarian Scientific Research Fund (OTKA) under grant Nos. 67893 and 81360. Á. Révész is indebted for the Bolyai Scholarship of the Hungarian Academy of Sciences, Zs. Kovács is grateful for the support of the Zoltán Magyary Fund and of the EEA Grants and Norway Grants. The authors are grateful to Dr. L.K. Varga for providing the amorphous ribbon, to Dr. A. Zhilyaev for the HPT disk and to Dr. P.J. Szabó for the SEM study. The authors acknowledge the European Synchrotron Radiation Facility for provision of synchrotron radiation facilities using beamline ID 11.

References

[1] H. Chen, Y. He, G.J. Shiflet, S.J. Poon, Nature 367 (1994) 541.
[2] Y. Zhang, A.L. Greer, Appl. Phys. Lett. 89 (2006) 071907.
[3] J.J. Lewandowski, A.L. Greer, Nat. Mater. 5 (2006) 15.
[4] C.A. Schuh, T.C. Hufnagel, U. Ramamurty, Acta Mater. 55 (2007) 4067.
[5] L.Q. Xing, Y. Li, K.T. Ramesh, J. Li, C. Hufnagel, Phys. Rev. B 64 (2001) 18020.
[6] X.K. Xi, D.Q. Zhao, M.X. Pan, W.H. Wang, Y. Wu, J.J. Lewandowski, Phys. Rev. Lett. 94 (2005) 125510.
[7] Y. Zhang, W.H. Wang, A.L. Greer, Nat. Mater. 5 (2006) 857.
[8] Y.H. Liu, G. Wang, R.J. Wang, D.Q. Zhao, M.X. Pan, W.H. Wang, Science 315 (2007) 1385.
[9] A. Inoue, N. Nishiyama, MRS Bull. 32 (2007) 651.
[10] A. Inoue, W. Zhang, T. Zhang, K. Kurosaka, J. Non-Cryst. Solids 304 (2002) 200.
[11] A. Concustell, M. Zielinska, Á. Révész, L.K. Varga, S. Suriñach, M.D. Baró, Intermetallics 12 (2004) 1063.
[12] D. Xu, B. Lohwongwatan, G. Duan, W.L. Johnson, C. Garland, Acta Mater. 52 (2004) 2621.
[13] S. Pauly, J. Bednarcik, U. Kühn, J. Eckert, Scr. Mater. 63 (2010) 336.
[14] S. Pauly, S. Gorantla, G. Wang, U. Kühn, J. Eckert, Nat. Mater. 9 (2010) 473.
[15] A.P. Zhilyaev, T.G. Langdon, Prog. Mater. Sci. 53 (2008) 893.
[16] N. Boucharat, H. Rösner, G. Wilde, J. Non-Cryst. Solids 354 (2008) 592.
[17] Zs. Kovács, P. Henits, A.P. Zhilyaev, Á. Révész, Scr. Mater. 54 (2006) 1733.
[18] Á. Révész, S. Hóbor, P.J. Szabó, A.P. Zhilyaev, Zs. Kovács, Mater. Sci. Eng. A 460–461 (2007) 459.
[19] R.Z. Valiev, R.K. Islamgaliev, I.V. Alexandrov, Prog. Mater. Sci. 45 (2000) 103.
[20] A.P. Zhilyaev, T.R. McNelley, T.G. Langdon, J. Mater. Sci. 42 (2007) 1517.
[21] M. Kawasaki, R.B. Figueiredo, T.G. Langdon, Acta Mater. 59 (2011) 308.
[22] X.H. An, S.D. Wu, Z.F. Zhang, R.B. Figueiredo, N. Gaob, T.G. Langdon, Scr. Mater. 63 (2010) 560.
[23] W. Dmowski, Y. Yokoyama, A. Chuang, Y. Ren, M. Umemoto, K. Tsuchiya, A. Inoue, T. Egami, Acta Mater. 58 (2010) 429.
[24] S. Hóbor, Á. Révész, P.J. Szabó, A.P. Zhilyaev, V. Kovács Kis, J.L. Lábár, Zs Kovács, J. Appl. Phys. 104 (2008) 033525.
[25] S. Hóbor, Zs. Kovács, Á. Révész, J. Alloys Compd. 495 (2010) 352.
[26] S. Hóbor, Zs. Kovács, Á. Révész, J. Appl. Phys. 106 (2009) 023531.
[27] S. Hóbor, Zs. Kovács, A.P. Zhilyaev, L.K. Varga, P.J. Szabó, Á. Révész, J. Phys.: Conf. Series 240 (2010) 012153.
[28] A. Hammersley, S.O. Svensson, A. Thompson, Nucl. Instrum. Methods A 346 (1994) 312.
[29] G.S. Fulcher, J. Am. Ceram. Soc. 6 (1925) 339.
[30] C.A. Angell, Science 267 (1995) 1924.
[31] R. Busch, JOM 52 (2000) 39.
[32] P. Henits, Á. Révész, L.K. Varga, Zs. Kovács, Intermetallics 19 (2011) 267.
[33] J.Z. Jiang, H. Kato, T. Ohsuna, J. Saida, A. Inoue, K. Saksl, H. Franz, K. Stahl, Appl. Phys. Lett. 83 (2005) 081913.